

# A neural network-based gravitational wave interpolant with applications to low-latency analyses

Ryan Magee <sup>1,\*</sup> Richard George <sup>2</sup> Alvin Li <sup>1</sup> and Ritwik Sharma <sup>3,4</sup>

<sup>1</sup>*LIGO, California Institute of Technology, Pasadena, CA 91125, USA*

<sup>2</sup>*Center for Gravitational Physics, University of Texas, Austin, TX 78712, USA*

<sup>3</sup>*Department of Physics, Deshbandhu College, University of Delhi, New Delhi, India*

<sup>4</sup>*STAR Lab, Indian Institute of Technology Bombay, Powai 400076, India*

Matched-filter based gravitational-wave search pipelines identify candidate events within seconds of their arrival on Earth, offering a chance to guide electromagnetic follow-up and observe multimessenger events. Understanding the detectors' response to an astrophysical transient across the searched signal manifold is paramount to inferring the parameters of the progenitor and deciding which candidates warrant telescope time. We describe a framework that uses artificial neural networks to interpolate gravitational waves and, equivalently, the signal-to-noise ratio (SNR) across sufficiently local patches of the signal manifold. Our machine-learning based model generates a single waveform in 6 milliseconds on a CPU and 0.4 milliseconds on a GPU. When using a GPU to generate batches of waveforms simultaneously, we find that we can produce  $10^4$  waveforms in  $\lesssim 1$  ms. This is achieved while remaining faithful, on average, to 1 part in  $10^4$  (1 part in  $10^5$ ) for binary black hole (binary neutron star) waveforms. The model we present is designed to directly utilize intermediate detection pipeline outputs in the hopes of facilitating a better real-time understanding of gravitational-wave candidates.

## I. INTRODUCTION

Gravitational-waves (GW) observed by Advanced LIGO [1] and Advanced Virgo [2] have provided an unprecedented view into our Universe. The candidates identified by the LIGO-Virgo-Kagra collaboration (LVK) [3] and external groups [4–11] provide an increasingly complete census of the ultracompact binaries in our universe [12]. Much of this science has been made possible by the low-latency search pipelines [13–17] that rapidly identifies GW candidates and the alert infrastructure [18, 19] that subsequently localizes and classifies them.

Binary neutron stars (BNSs) and neutron star – black hole binaries (NSBHs) remain particularly sought after since they are known [20, 21] (or, in the case of NSBHs, expected [22]) sources of electromagnetic radiation. It is therefore crucial to precisely understand the nature of compact binaries in near-real-time to determine which warrant electromagnetic followup. This is increasingly important as highly anticipated, next generation facilities like the Rubin Observatory [23] begin observations in the coming years. At present, our low-latency estimates of localization [24], classification [25–28], and source properties [22, 29] are derived from the highest signal-to-noise ratio (SNR) event among the maximum likelihood candidates identified by LVK detection pipelines. Though this results in precise localizations [30], it is well understood that full parameter estimation is systematically more accurate [19]. Unfortunately, even in their low-latency configuration, parameter estimation pipelines can take  $\mathcal{O}(\text{hours})$  to produce stable results, which may be too late to facilitate the capture of rapidly fading tran-

sients [31].

In this work, we examine neural networks as a way to interpolate the search response, in the hopes of developing a better real-time understanding of the nature of the candidate and enabling rapid parameter estimation in the future. Recently, machine-learning algorithms have emerged as a promising way to navigate GW science and other areas of data-driven astrophysics. This has largely been made possible by advances to graphical processing units (GPUs) and the ease of software that utilize them [32–34]. In GW astrophysics alone, machine-learning algorithms have already been applied to compact binary detection [35–42], early warning alerts [43–47], supernovae identification [48–50], parameter estimation [51–56], noise removal and characterization [57–59], and waveform interpolation [60–64].

Previous waveform interpolation applications have primarily focused on aligned-spin binary black holes (BBH) [60–62], though some have considered non-aligned systems as well [64]. Each of these works first converts the waveforms to a new basis, which is achieved via methods such as principal component analysis and Gram-Schmidt orthonormalization, before interpolating the coefficients needed to reconstruct the waveforms. In this work, we describe a similar technique. We employ neural networks trained via supervised learning to the interpolation of the GW emission and SNR of arbitrary aligned-spin compact binaries using singular value decomposition (SVD). This work is inspired by previous studies that used grid-based techniques to interpolate the SVD of nonspinning BBH signals [65], as well as mesh-free approaches applied to the SVD of aligned-spin BNS emission [66]. We build on previous SVD interpolation efforts and additionally consider the impacts of component spin, interpolate waveforms of arbitrary length, and provide a method that is immediately applicable to existing

---

\* [rmmagee@caltech.edu](mailto:rmmagee@caltech.edu)

low-latency analyses and requires minimal fine tuning. The interpolant we describe provides a way to rapidly calculate the SNR of aligned-spin compact binaries, which may be able to accelerate low-latency data enrichment tasks.

This paper is organized as follows. First, we describe the matched-filtering algorithms and neural network architecture in Section II. Second, we apply this network to BBH and BNS systems. We describe the accuracy of the interpolant on these systems and present a timing study in Section III. Finally, we conclude with a discussion of future applications in low-latency environments in Section IV.

## II. METHODS

### A. Background and motivation

Modern matched-filter based GW pipelines simultaneously search for GWs from BNS, BBH, and NSBH binaries. The searches precompute the expected gravitational wave emission, also known as a *template*, for  $\mathcal{O}(10^6)$  binaries representative of the space. This collection of templates, or *template bank*, is designed to retain 97%–99% of the SNR. While the overall parameter space is vast, pipelines often divide their search across a number of small, partially-overlapping *sub-banks* in the signal manifold that contain templates with morphologies [67–69] that respond similarly to astrophysical sources and detector noise.

The similarities between the waveforms in a sub-bank can be exploited by using *singular value decomposition* (SVD) [68, 70] to reduce the filtering cost of the search. The SVD ensures that we can express any of the  $N^1$  waveforms within our sub-bank as a sum of some orthogonal basis vectors,  $u_\mu(t)$ , and complex-valued reconstruction coefficients,  $a(\lambda)_\mu$ :

$$h(\lambda, t) = \sum_{\mu=0}^M a(\lambda)_\mu u_\mu(t) \quad (1)$$

where  $\lambda = (m_1, m_2, s_{1z}, s_{2z})$  represents the set of intrinsic parameters of the system,  $h(\lambda, t)$  is the whitened gravitational-wave strain for parameters  $\lambda$  at time  $t$ ,  $M$  represents the number of bases identified by the SVD, and  $M \leq N$ . We neglect the impact of the location and orientation of the binary on the GW emission, which can be applied via a complex rotation for aligned-spin systems. Further approximations can be applied to ensure that  $M \ll N$ , which greatly reduces the number of filters a search must correlate with the data. We refer the

reader to [70] for a complete description of this method applied to compact binary searches.

A further speed up can be achieved by first segmenting the waveforms into distinct time-slices and downsampling within each slice to the Nyquist rate associated with the highest frequency component:

$$h(\lambda, k) = \sum_{s=0}^{S-1} \begin{cases} h(\lambda, k \frac{f}{f^s})^s & t^s \leq k/f^s < t^{s+1} \\ 0 & \text{else} \end{cases} \quad (2)$$

where  $h(\lambda, t)^s$  is the whitened gravitational-wave strain at time  $t$  in time slice  $s$ ,  $f^s$  is the sample-rate in the corresponding time slice, and  $S$  is the total number of time slices.

Each time slice is independent of the next, and a SVD can be performed on each individually to identify orthonormal bases for each segment:

$$h(\lambda, t)^s = \sum_{\mu=0}^{M-1} a_\mu^s(\lambda) u_\mu^s(t) \quad (3)$$

Here,  $a_\mu^s(\lambda)$  denotes the complex<sup>2</sup> valued reconstruction coefficient associated with basis vector  $\mu$  and time slice  $s$ ,  $u_\mu^s(t)$  is the basis vector for time slice  $s$ , and  $M$  is the number of basis vectors associated with time slice  $s$ . This process is known as the Low Latency Online Inspiral Detection (LLOID) algorithm, and it is currently employed within the GstLAL-based detection pipeline. An comprehensive description of the LLOID algorithm can be found in [71]. A similar, frequency domain procedure is used by MBTA [72].

Previous studies have provided numerical evidence that bases produced by SVD are complete over the signal manifold from which they were derived [73]. Our goal in this work is exploit that completeness and to use machine learning to faithfully interpolate the reconstruction coefficients  $a_\mu^s(\lambda)$  for any  $\lambda$  contained within the corresponding sub-bank. Note that under the LLOID framework, the SNR time series can be written as:

$$\rho(\lambda, t)^s = \langle h(\lambda, t)^s | d(t) \rangle = \sum_{\mu=0}^{M-1} a_\mu^s(\lambda) \langle u_\mu^s(t) | d \rangle \quad (4)$$

where,  $\langle \cdot | \cdot \rangle$  denotes the noise weighted inner product

$$\langle a(t) | b(t) \rangle \equiv 4 \int_0^\infty df \frac{a^*(f) b(f)}{S_n(f)} \quad (5)$$

for the one-sided power spectral density (PSD),  $S_n(f)$ . The final term in equation 4,  $\langle u_\mu^s(t) | d(t) \rangle$ , is the orthogonal SNR measured directly by the pipeline. The SNR corresponding to the physical template,  $\rho$ , is reconstructed

<sup>1</sup> Performing an SVD on large matrices is known to be computationally expensive. Within the GstLAL framework, searches set  $N \leq 1024$  to reduce cost.

<sup>2</sup> The complex valued coefficient encodes the two polarizations of a GW under general relativity.

via matrix multiplication. Interpolating the reconstruction coefficients  $a_\mu^s(\lambda)$  is therefore equivalent to producing arbitrary waveforms *and* arbitrary SNR timeseries since both utilize the same coefficients. Interpolating the SNRs across the signal manifold exposes more information than would otherwise be available from the small, discrete space sampled by the search, and will enrich our understanding of the properties of low-latency GW candidates.

## B. Machine learning architecture

We use a feed-forward neural network as a form of supervised learning to derive the relationship between our four inputs,  $\lambda$ , and our two real-valued outputs per basis vector,  $\text{Re } a_\mu^s(\lambda)$  and  $\text{Im } a_\mu^s(\lambda)$ . Such networks consist of three types of layers (input, hidden, and output), where each layer contains nodes, or *neurons*, that are fully connected to adjacent layers of arbitrary size. The input to any layer can be represented by a vector  $\vec{x}$  with dimensionality equal to the number of neurons. The interaction between a layer with input size  $N$  and output size  $M$  can be completely characterized by a weight matrix,  $W$ , with dimension  $N \times M$ , a bias vector,  $\vec{b}$ , and an activation function,  $f(x)$ , which is typically non-linear and is applied to each output neuron individually. The weight matrix describes the strength of the connection between any two neurons in adjacent layers, while the bias term provides added flexibility to the model by providing an offset. The output for a given neuron is then

$$\vec{y} = f(W^T \vec{x} + \vec{b}) \quad (6)$$

where  $\vec{y}$  has dimension  $M$ .

The weights and biases that describe a network are not set initially, but learned via supervised training. This learning occurs by minimizing a loss function that compares the target training data to the network output; the most commonly used loss function for regression-based tasks such as the one described here is the mean-square error,

$$\text{MSE} = \frac{1}{n} \sum_{i=0}^n (y_i - \hat{y}_i)^2 \quad (7)$$

where  $y_i$  and  $\hat{y}_i$  are the expected values from the training data and the network outputs, respectively, and  $n$  denotes the size of the dataset.

The appropriate choice for the number of layers, neurons per layer, and activation function can vary depending on the task, though there are a number of key features that are typically desired. Continuous differentiability, monotonicity, and fixed output ranges are generally preferred since they facilitate network backpropagation, gradient descent, and learning stability, and can ameliorate the vanishing or exploding gradient problem [74]. In this work, we use the network to perform regression and estimate a set of weights that describes the contribution

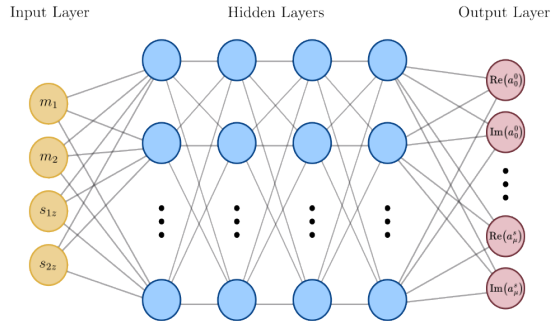


FIG. 1. A schematic of the neural network architecture used in this work. The network takes the intrinsic parameters  $\lambda = (m_1, m_2, s_{1z}, s_{2z})$  as input and returns the reconstruction coefficients  $a_\mu^s(\lambda)$  as output. Our network has two outputs per basis vector, representing the two polarizations of the GW. The total number of outputs depends on the number of time slices and SVD bases needed for a particular sub-bank.

for a number of basis vectors. We use a neural network consisting of a 4-node input layer corresponding to  $\lambda = (m_1, m_2, s_{1z}, s_{2z})$ , 4 hidden layers of 512 neurons, and an output layer whose size depends on the total number of basis vectors contained in a specific sub-bank (Fig. 1). For our data, each time slice is independent of the next, so we have the freedom to fit each segment of the waveform separately. Similarly, we could train each basis vector independently. Instead, we elect to fit all time slices and bases at once to reduce the total number of models needed. We use Rectified Linear Units (ReLUs) as the activation function for our hidden layers, defined as

$$f(x) = \max(0, x). \quad (8)$$

We use the mean-square error as our loss function, and the Adam optimizer [75] to minimize the loss function. We choose to use  $\lambda$  as the input to our network to highlight the generality of this method, but we note that transforming coordinates to the parameters most important for the phasing of the signal [76, 77] could lead to more accurate or faster converging results. We do not exclude the possibility that another set of coordinates may be necessary in regions of the parameter space that exhibit significant degeneracies.

## III. STUDY

### A. Fidelity

We apply the above formalism to BNS and BBH systems. We generate small BNS and BBH banks with minimum matches [78] of 0.99 using a stochastic placement algorithm [79, 80]. The banks are not intended

to be representative of a full GW search; rather, they are constructed in a constrained section of the parameter space to be illustrative of sub-bank grouping in current low-latency analyses. We refer the reader to Figures 2 and 4 in [81] and [69], respectively, for grouping visualizations. The BBH (BNS) bank is designed to recover compact binaries with  $20M_{\odot} < m_2 \leq m_1 < 40M_{\odot}$  ( $1.40M_{\odot} < m_2 \leq m_1 < 1.42M_{\odot}$ ) and  $0.5 < s_{iz} < 0.75$  ( $0.00 < s_{iz} < 0.01$ ), where  $m_1, m_2$  are the component masses of the binary and  $s_{1z}, s_{2z}$  are the components of the spin angular momentum aligned with the orbital angular momentum. The resulting bank contains 193 (343) waveforms. We verify the coverage of the banks by drawing  $10^4$  random samples from within the bounds and computing the mismatches,

$$\mathcal{M}(h_i, h_j) \equiv 1 - \frac{\langle h_i | h_j \rangle}{\langle h_i | h_i \rangle \langle h_j | h_j \rangle} \quad (9)$$

between each sample and every template within the respective bank. In each case, no simulation has a mismatch  $\geq .011$  with some template in the bank. The median mismatch across all simulations is 0.002 (0.003) for the BBH (BNS) bank.

We model the gravitational wave emission in each bank using the `SEOBNRv4_ROM (TaylorF2)` waveform approximants [82, 83], which are presently used to model the BBH (BNS) region of the `GstLAL` template bank in Advanced LIGO, Advanced Virgo, and KAGRA’s fourth observing run [69]. The emission is modeled from a starting frequency of 20 Hz (32 Hz) to capture the entirety of the BBH signals and the last minute of the BNS signals in the detectors’ sensitive bands. For each bank, we use the `LLOID` algorithm to first segment the waveforms in time, and then to find a set of orthogonal basis vectors for each time-slice. This yields 2 (7) time slices with a total of 62 (80) basis vectors distributed across them.

Ultimately, our network aims to predict  $a_{\mu}^s(\lambda)$  for each basis,  $\mu$ , and time slice,  $s$ . To construct data to train our machine-learning model, we uniformly draw  $10^5$  samples from the 4-dimensional hyper-rectangle defined by the boundaries of each template bank. Similar work [84] has utilized Latin Hypercube sampling [85] to provide samples that are representative of variability within the hypercube. Since our interpolant is meant to act in a highly parallel fashion and over local areas of the signal manifold where there is not substantial metric variability, we find that random sampling suffices. We segment and whiten each waveform using the publicly available `aligo04_low.txt` estimate of Advanced LIGO’s power spectral density for the fourth observing run<sup>3</sup>. We rotate the waveforms so that the phase at the time of peak amplitude is zero<sup>4</sup>, and then project each waveform segment onto the corresponding basis vector obtained from

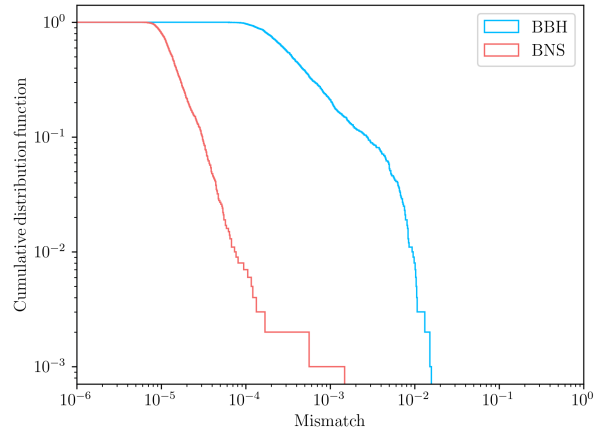


FIG. 2. Reconstruction accuracy of the neural-net interpolated waveform for BBH and BNS systems. All interpolated waveforms have a mismatch no worse than one part in  $10^2$  ( $10^3$ ) and, on average, 1 part in  $10^4$  ( $10^5$ ) for BBH (BNS), which is at the level of waveform systematics.

the SVD to obtain the complex valued reconstruction coefficients associated with each time slice and basis:

$$a_{\mu}^s(\lambda) = h^s(\lambda, t) \cdot u_{\mu}^s(t) \quad (10)$$

We store the reconstruction coefficients as a pair of real-valued numbers,  $\text{Re } a_{\mu}^s(\lambda)$  and  $\text{Im } a_{\mu}^s(\lambda)$ . The number of coefficients needed to reconstruct the original waveform scales with the numbers of bases and the number of time slices. Though in general this quantity changes across the parameter space, it remains constant within a single decomposed bank.

We train a neural network for each bank separately using the architecture described in Section II B. We find that both the BBH and BNS models are computed in  $\lesssim 10$  minutes on a GPU. The performance of the resulting models are summarized in Fig. 2. We find that our BBH (BNS) model achieves a median mismatch of  $10^{-4}$  ( $10^{-5}$ ). The worst mismatch is  $10^{-2}$  ( $10^{-3}$ ), which is of the order of waveform systematics [82]. The worst reconstructed waveforms are shown in Figure 3a and 3b alongside their phase residuals.

## B. Waveform and SNR interpolation timing study

The frequency domain, aligned spin waveform models `TaylorF2` and `SEOBNRv4_ROM` can be generated in 1.1 ms and 2.5 ms, respectively, on a central processing unit (CPU) using `LALSuite` waveform calls. Recent work [86] has examined accelerating waveform generation with `JAX` [87], producing an aligned-spin waveform in 0.4 ms on a CPU (0.14 ms with `vmap` integration) and 0.02 ms on a GPU. Other works have also applied neural networks to aligned-spin BBH waveforms, finding that they can be produced in 0.1 ms – 5 ms on GPUs [60–62]

<sup>3</sup> <https://dcc.ligo.org/LIGO-T2000012/public>.

<sup>4</sup> This convention is chosen so that our interpolated waveforms all have phase zero and can be trivially rotated to arbitrary phase.

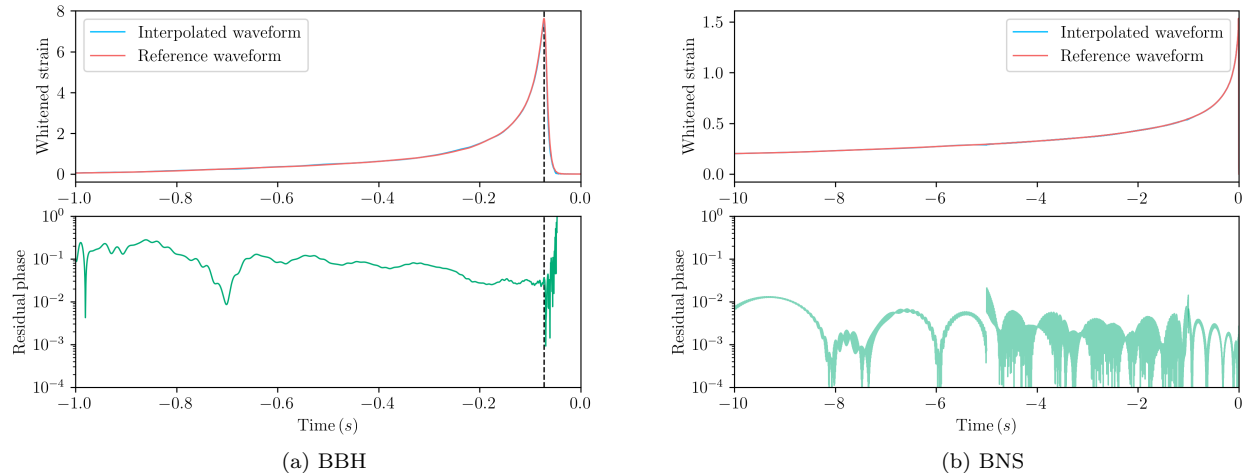


FIG. 3. Two representative interpolated waveforms and the associated residual phase. The vertical dashed line in the left plot indicates the merger time for the BBH. The pre-merger BBH phase agrees to approximately 1 part in  $10^1 - 10^2$ , while the BNS phase agrees to 1 part in  $10^2 - 10^4$ . This shows that the interpolant provided here accurately reconstructs both the amplitude and phase of arbitrary signals.

We find that the neural network based interpolant described here has similar performance to the above methods when utilizing accelerated linear algebra [34] and just-in-time compilation. We summarize our findings in Table I. We find that we can produce a single waveform in 0.5 ms on a CPU and 0.3 ms in a GPU. GPUs also offer the ability to batch waveform generation. On an A100 GPU, we find that we can produce  $10^4$  waveforms in  $\sim 0.8$  ms, which corresponds to an effective speed of 1 waveform per 80 ns. The waveform generation time is roughly independent of signal length since the size of the output layer size remains approximately constant across banks. In all cases, we randomly sample from within the confines of the reference template bank.

Recall that under our chosen framework, generating a GW via a weighted average of SVD bases is equivalent to calculating the SNR timeseries using a weighted average of SNR timeseries collected for each orthogonal basis found by the SVD (see Equation 4). The timings described in Table I are thus also representative of how long it takes to calculate an arbitrary SNR using the orthogonal SNRs output by the LLOID algorithm in low-latency. For reference, we compare to the cost of performing this correlation on a CPU with Bilby [88]. Table II shows the average time to compute  $\langle h(t)|d(t) \rangle$  in the frequency domain for a fiducial 16 s (64 s) BBH (BNS) waveforms at 5 different sample rates. Naively comparing our timing results to those of Bilby indicate a 1 – 30 time speed-up for a single SNR calculation and an  $\mathcal{O}(10^4 - 10^5)$  speed-up for calculations batched on a GPU. In each case, we compare the time to produce an SNR value when either Bilby or our method is evaluated at a known point in the parameter space. This method is similar to reduced-order-quadrature (ROQ) techniques [77, 89, 90], which

offer similar accelerations for much broader signal manifolds than the ones considered here, though these are not directly integrated into the detection process.

### C. Signal loss from PSD drift

Since the basis vectors are constructed via SVD on the *whitened* gravitational waveforms, changes in the measured PSD fundamentally alter the bases and can lead to signal loss. To minimize bias, the low-latency GstLAL analysis recomputes the bases on a weekly cadence with updated PSDs. While in principle, the same should be done for our method, we find it to be a small effect in practice. To estimate the impact, we use the more optimistic, publicly available `aligo04_high.txt` PSD estimate for O4<sup>5</sup>. This is an extreme case of PSD drift since the new PSD represents a detector that is 12.5% more sensitive. We use this as a proxy for PSD evolution over the course of the run. With this new PSD, we generate 1000 sample whitened waveforms and compare to the waveforms predicted by our neural network. We find that models trained on the less sensitive PSD still reproduce the correct waveform to within 1 part in  $10^2$  ( $10^3$ ). These results are shown in Figure 4. This is still within the range of waveform systematics, though we do not rule out the possibility that specific, frequency dependent PSD changes could lead to more substantial differences.

<sup>5</sup> This PSD is also available at [and](#) represents LIGO detectors that are 12.5% more sensitive than those described by `aligo04_low.txt`

	CPU	GTX 1080	A100
	Total time (Time per waveform)	Total time (Time per waveform)	Total time (Time per waveform)
Single BBH	0.52 (0.52)	0.40 (0.40)	0.28 (0.28)
Batched ( $10^4$ ) BBHs	28 (.0028)	3.6 (.00036)	0.84 (.000084)
Single BNS	0.11 (0.11)	0.41 (0.41)	0.29 (0.29)
Batched ( $10^4$ ) BNSs	27 (.0027)	3.5 (.00035)	0.9 (.00009)

TABLE I. Approximate times in milliseconds to generate our interpolated version of `TaylorF2` waveforms for BNS (top) and `SEOBNRv4_ROM` waveforms BBH (bottom) systems on a consumer and industry grade GPU. Timing results are averaged over  $10^4$  independent calls for both single and batched waveforms. The evaluation time is approximately constant across waveform length since the number of coefficients needed to reconstruct waveforms remains of the same order of magnitude.

	TaylorF2	SEOBNRv4_ROM	IMRPhenomD
	(64s)	(16s)	(16s)
2048 Hz	6.2	6.7	5.1
1024 Hz	4.0	5.1	3.1
512 Hz	2.5	3.1	1.7
256 Hz	2.0	3.2	1.9
128 Hz	1.5	3.6	0.6
Speed-up (single)	5 – 21	13 – 24	-
Speed-up (batched)	$\mathcal{O}(10^4)$	$\mathcal{O}(10^4)$	-

TABLE II. Approximate time in milliseconds to generate a waveform and compute  $\langle h|d \rangle$  in the frequency domain with `Bilby`. Each row corresponds to waveforms generated at different sample rates, while the column denotes a specific waveform family and signal duration. We provide results for a variety of sample rates to reflect that our method uses time-sliced and downsampled waveforms at intermediate steps. In all cases, we fix the detector response and only profile waveform generation and the inner product calculation. In our framework, waveform generation is equivalent to reconstructing physical SNRs from SNRs measured by the SVD bases. A naive comparison of our model’s waveform generation time in Table I to the extreme sample rates shown here suggests that single waveform SNR calculations can be accelerated by factors of a few to tens. When using batched generation, the acceleration is more extreme; note that this assumes the `Bilby` calls are still done in serial.

In the case of model breaking PSD changes, our network can be asynchronously updated and retrained with the new spectrum. We leave a study of potential biases on parameter estimation to a future work.

#### IV. CONCLUSION AND FUTURE WORK

In this work, we have presented a neural network based interpolant for GWs connected to existing low-latency detection algorithms and data products. This method allows us to accelerate the production of GWs and their associated SNR time-series by up to a factor of  $10^4$  for aligned spin binary systems while retaining a faithfulness, on average, of 1 part in  $10^4(10^5)$  to the original whitened BBH (BNS) waveforms. Although changes in the detector noise properties reduce our model’s fidelity, we find that it is still accurate to within the level of waveform systematics. The interpolant is constructed in a highly parallel fashion to mimic how matched-filter based search pipelines split the target parameter space to efficiently carry out low-latency analyses. This leads to models that train in  $\sim 10$  minutes. Modern searches cover much broader parameter spaces than the two re-

gions we consider here; we estimate that it would take  $\sim 1$  week to train models in serial on a single GPU to cover the full parameter space associated with matched-filter based analyses [69].

In low-latency, the `GstLAL` search pipeline functions as a collection of microservices that loosely communicate with one another. Each microservice controls the filtering (among other tasks) for small groups of sub-banks. The microservices perform matched filtering in the reduced space described by the SVD bases, but combine these outputs to provide a physical SNR associated with the parameters of some template within the bank. This work shows that the intermediate SNRs collected by the basis vectors can be mapped to arbitrary points in the sub-bank in near-real-time. If a new microservice is created to ingest small snippets of intermediate SNRs from each filtering job, then the lightweight model described here can be used to rapidly estimate the SNRs at arbitrary points in the search space. This effectively amortizes the costly likelihood calculation utilized by Bayesian inference based parameter estimation pipelines and provides the SNR time-series across the search space at arbitrary density.

This has the potential to both accelerate and im-

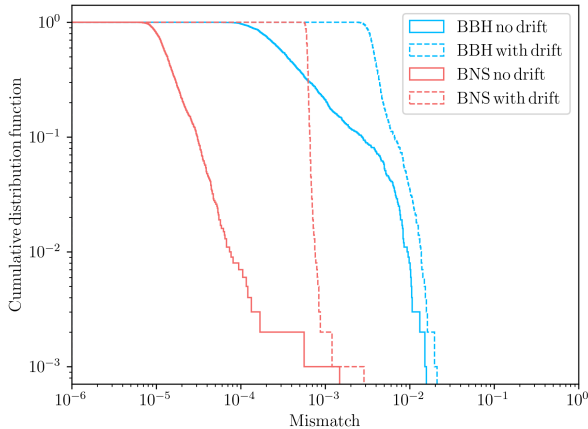


FIG. 4. The mismatch distribution for interpolated BNS waveforms for the PSD used in this work (blue) and a more sensitive one (orange). While the bulk of the distribution shifts towards higher mismatches, the interpolated waveforms remain accurate to 1 part in  $10^2$  ( $10^3$ ) and the median mismatches remain of the same order of magnitude as before. This is still of the order of expected disagreement between different waveform families, suggesting that the models are still appropriate for use.

prove the accuracy of near-real-time parameter estimation based tasks. Low-latency localization is performed using BAYESTAR [24], which fixes the masses and spins to the maximum search likelihood estimate and performs Bayesian inference over the extrinsic parameters. Though accurate, it is well known that full parameter estimation produces systematically more accurate skymaps, albeit at significantly greater computational cost. SNR interpolation would allow algorithms such as BAYESTAR to marginalize over masses and spins to achieve a higher accuracy. Alternatively, it could be used to maximize the SNR via brute-force. After identifying candidates in low-latency, some detection pipelines employ an SNR optimization task to scan the local parameter space for slightly louder triggers. This interpolator could be used similarly, while probing a much denser space than current algorithms. While this will likely identify candidates with  $\lesssim 1\%$  higher SNR, it will still lead to systematically tighter localizations.

Source classification using Bayesian inference is presently done with medium latency ( $\mathcal{O}(\text{minutes})$ ) algorithms that perform full parameter estimation [91, 92], but it is possible that these could be accelerated even more with our interpolant. These algorithms exploit the separability of aligned-spin gravitational wave signals to efficiently evaluate the GW likelihood for arbitrary extrinsic parameters. The method described here could similarly accelerate likelihood evaluations at arbitrary intrinsic parameters. Future work will discuss the connection of this technique to the RAPIDPE algorithm [91, 93], which utilizes adaptive mesh refinement [94], in the pur-

suit of  $\mathcal{O}(\text{seconds})$  parameter estimation.

Finally, since the mapping between bases and physical parameters is possible, it is also intriguing to consider if the response from the reduced bases can be used with likelihood-free methods [95] to amortize inference entirely. Some parameter estimation algorithms already utilize similar techniques [52, 96]. We leave this study for future work.

## ACKNOWLEDGMENTS

The authors thank Jacob Golomb for Bilby assistance and useful comments. LIGO was constructed by the California Institute of Technology and Massachusetts Institute of Technology with funding from the National Science Foundation and operates under cooperative agreement PHY-1764464. This research has made use of data, software and/or web tools obtained from the Gravitational Wave Open Science Center (<https://www.gwopenscience.org>), a service of LIGO Laboratory, the LIGO Scientific Collaboration and the Virgo Collaboration. Virgo is funded by the French Centre National de Recherche Scientifique (CNRS), the Italian Istituto Nazionale della Fisica Nucleare (INFN) and the Dutch Nikhef, with contributions by Polish and Hungarian institutes. This material is based upon work supported by NSF’s LIGO Laboratory which is a major facility fully funded by the National Science Foundation. The authors are grateful for computational resources provided by the LIGO Laboratory and supported by NSF Grants PHY-0757058 and PHY-0823459. This research has made use of data or software obtained from the Gravitational Wave Open Science Center ([gwosc.org](http://gwosc.org)), a service of LIGO Laboratory, the LIGO Scientific Collaboration, the Virgo Collaboration, and KAGRA. This paper carries LIGO document number LIGO-P2400308.

- [1] J. Aasi *et al.* (LIGO Scientific), *Class. Quant. Grav.* **32**, 074001 (2015), [arXiv:1411.4547 \[gr-qc\]](#).
- [2] F. Acernese *et al.* (VIRGO), *Class. Quant. Grav.* **32**, 024001 (2015), [arXiv:1408.3978 \[gr-qc\]](#).
- [3] R. Abbott *et al.* (LIGO Scientific, VIRGO, KAGRA), (2021), [arXiv:2111.03606 \[gr-qc\]](#).
- [4] A. H. Nitz, C. Capano, A. B. Nielsen, S. Reyes, R. White, D. A. Brown, and B. Krishnan, *Astrophys. J.* **872**, 195 (2019), [arXiv:1811.01921 \[gr-qc\]](#).
- [5] R. Magee *et al.*, *Astrophys. J. Lett.* **878**, L17 (2019), [arXiv:1901.09884 \[gr-qc\]](#).
- [6] T. Venumadhav, B. Zackay, J. Roulet, L. Dai, and M. Zaldarriaga, *Phys. Rev. D* **101**, 083030 (2020), [arXiv:1904.07214 \[astro-ph.HE\]](#).
- [7] B. Zackay, L. Dai, T. Venumadhav, J. Roulet, and M. Zaldarriaga, *Phys. Rev. D* **104**, 063030 (2021), [arXiv:1910.09528 \[astro-ph.HE\]](#).
- [8] A. H. Nitz, T. Dent, G. S. Davies, S. Kumar, C. D. Capano, I. Harry, S. Mozzon, L. Nuttall, A. Lundgren, and M. Tápai, *Astrophys. J.* **891**, 123 (2020), [arXiv:1910.05331 \[astro-ph.HE\]](#).
- [9] A. H. Nitz, C. D. Capano, S. Kumar, Y.-F. Wang, S. Kastha, M. Schäfer, R. Dhurkunde, and M. Cabero, *Astrophys. J.* **922**, 76 (2021), [arXiv:2105.09151 \[astro-ph.HE\]](#).
- [10] A. H. Nitz, S. Kumar, Y.-F. Wang, S. Kastha, S. Wu, M. Schäfer, R. Dhurkunde, and C. D. Capano, *Astrophys. J.* **946**, 59 (2023), [arXiv:2112.06878 \[astro-ph.HE\]](#).
- [11] S. Olsen, T. Venumadhav, J. Mushkin, J. Roulet, B. Zackay, and M. Zaldarriaga, *Phys. Rev. D* **106**, 043009 (2022), [arXiv:2201.02252 \[astro-ph.HE\]](#).
- [12] R. Abbott *et al.* (KAGRA, VIRGO, LIGO Scientific), *Phys. Rev. X* **13**, 011048 (2023), [arXiv:2111.03634 \[astro-ph.HE\]](#).
- [13] L. Tsukada *et al.*, *Phys. Rev. D* **108**, 043004 (2023), [arXiv:2305.06286 \[astro-ph.IM\]](#).
- [14] A. H. Nitz, T. Dal Canton, D. Davis, and S. Reyes, *Phys. Rev. D* **98**, 024050 (2018), [arXiv:1805.11174 \[gr-qc\]](#).
- [15] F. Aubin *et al.*, *Class. Quant. Grav.* **38**, 095004 (2021), [arXiv:2012.11512 \[gr-qc\]](#).
- [16] Q. Chu *et al.*, *Phys. Rev. D* **105**, 024023 (2022), [arXiv:2011.06787 \[gr-qc\]](#).
- [17] M. Drago *et al.*, (2020), [arXiv:2006.12604 \[gr-qc\]](#).
- [18] R. Magee *et al.*, *Astrophys. J. Lett.* **910**, L21 (2021), [arXiv:2102.04555 \[astro-ph.HE\]](#).
- [19] S. S. Chaudhary *et al.*, *Proc. Nat. Acad. Sci.* **121**, e2316474121 (2024), [arXiv:2308.04545 \[astro-ph.HE\]](#).
- [20] B. P. Abbott *et al.* (LIGO Scientific, Virgo), *Phys. Rev. Lett.* **119**, 161101 (2017), [arXiv:1710.05832 \[gr-qc\]](#).
- [21] B. P. Abbott *et al.* (LIGO Scientific, Virgo, Fermi GBM, INTEGRAL, IceCube, AstroSat Cadmium Zinc Telluride Imager Team, IPN, Insight-Hxmt, ANTARES, Swift, AGILE Team, 1M2H Team, Dark Energy Camera GW-EM, DES, DLT40, GRAWITA, Fermi-LAT, ATCA, ASKAP, Las Cumbres Observatory Group, OzGrav, DWF (Deeper Wider Faster Program), AST3, CAAS-TRO, VINROUGE, MASTER, J-GEM, GROWTH, JAGWAR, CaltechNRAO, TTU-NRAO, NuSTAR, Pan-STARRS, MAXI Team, TZAC Consortium, KU, Nordic Optical Telescope, ePESSTO, GROND, Texas Tech University, SALT Group, TOROS, BOOTES, MWA, CALET, IKI-GW Follow-up, H.E.S.S., LOFAR, LWA, HAWC, Pierre Auger, ALMA, Euro VLBI Team, Pi of Sky, Chandra Team at McGill University, DFN, ATLAS Telescopes, High Time Resolution Universe Survey, RIMAS, RATIR, SKA South Africa/MeerKAT), *Astrophys. J. Lett.* **848**, L12 (2017), [arXiv:1710.05833 \[astro-ph.HE\]](#).
- [22] F. Foucart, T. Hinderer, and S. Nissanke, *Phys. Rev. D* **98**, 081501 (2018).
- [23] v. Z. Ivezić *et al.* (LSST), *Astrophys. J.* **873**, 111 (2019), [arXiv:0805.2366 \[astro-ph\]](#).
- [24] L. P. Singer and L. R. Price, *Phys. Rev. D* **93**, 024013 (2016), [arXiv:1508.03634 \[gr-qc\]](#).
- [25] W. M. Farr, J. R. Gair, I. Mandel, and C. Cutler, *Physical Review D* **91**, 023005 (2015), [arXiv:1302.5341 \[astro-ph.IM\]](#).
- [26] S. J. Kapadia *et al.*, *Class. Quant. Grav.* **37**, 045007 (2020), [arXiv:1903.06881 \[astro-ph.HE\]](#).
- [27] N. Andres *et al.*, *Class. Quant. Grav.* **39**, 055002 (2022), [arXiv:2110.10997 \[gr-qc\]](#).
- [28] V. Villa-Ortega, T. Dent, and A. C. Barroso, *Mon. Not. Roy. Astron. Soc.* **515**, 5718 (2022), [arXiv:2203.10080 \[astro-ph.HE\]](#).
- [29] S. Ghosh, X. Liu, J. Creighton, I. M. n. Hernandez, W. Kastaun, and G. Pratten, *Phys. Rev. D* **104**, 083003 (2021).
- [30] L. P. Singer *et al.*, *Astrophys. J.* **795**, 105 (2014), [arXiv:1404.5623 \[astro-ph.HE\]](#).
- [31] P. S. Cowperthwaite *et al.*, *Astrophys. J. Lett.* **848**, L17 (2017), [arXiv:1710.05840 \[astro-ph.HE\]](#).
- [32] NVIDIA, P. Vingelmann, and F. H. Fitzek, “Cuda, release: 10.2.89,” (2020).
- [33] A. Paszke, S. Gross, F. Massa, A. Lerer, J. Bradbury, G. Chanan, T. Killeen, Z. Lin, N. Gimelshein, L. Antiga, A. Desmaison, A. Kopf, E. Yang, Z. DeVito, M. Raison, A. Tejani, S. Chilamkurthy, B. Steiner, L. Fang, J. Bai, and S. Chintala, in *Advances in Neural Information Processing Systems 32* (Curran Associates, Inc., 2019) pp. 8024–8035.
- [34] A. Sabne, “XLA : Compiling Machine Learning for Peak Performance,” (2020).
- [35] D. George and E. A. Huerta, *Phys. Lett. B* **778**, 64 (2018), [arXiv:1711.03121 \[gr-qc\]](#).
- [36] H. Gabbard, M. Williams, F. Hayes, and C. Messenger, *Phys. Rev. Lett.* **120**, 141103 (2018), [arXiv:1712.06041 \[astro-ph.IM\]](#).
- [37] M. B. Schäfer *et al.*, *Phys. Rev. D* **107**, 023021 (2023), [arXiv:2209.11146 \[astro-ph.IM\]](#).
- [38] T. Mishra *et al.*, *Phys. Rev. D* **105**, 083018 (2022), [arXiv:2201.01495 \[gr-qc\]](#).
- [39] P. G. Krastev, *Phys. Lett. B* **803**, 135330 (2020), [arXiv:1908.03151 \[astro-ph.IM\]](#).
- [40] M. B. Schäfer, F. Ohme, and A. H. Nitz, *Phys. Rev. D* **102**, 063015 (2020), [arXiv:2006.01509 \[astro-ph.HE\]](#).
- [41] P. Nousi, A. E. Koloniari, N. Passalis, P. Iosif, N. Stergioulas, and A. Tefas, *Phys. Rev. D* **108**, 024022 (2023), [arXiv:2211.01520 \[gr-qc\]](#).
- [42] E. Marx *et al.*, (2024), [arXiv:2403.18661 \[gr-qc\]](#).
- [43] W. Wei and E. A. Huerta, *Phys. Lett. B* **816**, 136185 (2021), [arXiv:2010.09751 \[gr-qc\]](#).

- [44] G. Baltus, J. Janquart, M. Lopez, A. Reza, S. Caudill, and J.-R. Cudell, *Phys. Rev. D* **103**, 102003 (2021), [arXiv:2104.00594 \[gr-qc\]](#).
- [45] H. Yu, R. X. Adhikari, R. Magee, S. Sachdev, and Y. Chen, *Phys. Rev. D* **104**, 062004 (2021), [arXiv:2104.09438 \[gr-qc\]](#).
- [46] G. Baltus, J. Janquart, M. Lopez, H. Narola, and J.-R. Cudell, *Phys. Rev. D* **106**, 042002 (2022), [arXiv:2205.04750 \[gr-qc\]](#).
- [47] R. Alfaidi and C. Messenger, (2024), [arXiv:2402.04589 \[gr-qc\]](#).
- [48] P. Astone, P. Cerdá-Durán, I. Di Palma, M. Drago, F. Muciaccia, C. Palomba, and F. Ricci, *Phys. Rev. D* **98**, 122002 (2018), [arXiv:1812.05363 \[astro-ph.IM\]](#).
- [49] J. M. Antelis, M. Cavaglia, T. Hansen, M. D. Morales, C. Moreno, S. Mukherjee, M. J. Szczepańczyk, and M. Zanolin, *Phys. Rev. D* **105**, 084054 (2022), [arXiv:2111.07219 \[gr-qc\]](#).
- [50] M. López Portilla, I. D. Palma, M. Drago, P. Cerdá-Durán, and F. Ricci, *Phys. Rev. D* **103**, 063011 (2021), [arXiv:2011.13733 \[astro-ph.IM\]](#).
- [51] H. Gabbard, C. Messenger, I. S. Heng, F. Tonolini, and R. Murray-Smith, *Nature Phys.* **18**, 112 (2022), [arXiv:1909.06296 \[astro-ph.IM\]](#).
- [52] M. Dax, S. R. Green, J. Gair, J. H. Macke, A. Buonanno, and B. Schölkopf, *Phys. Rev. Lett.* **127**, 241103 (2021), [arXiv:2106.12594 \[gr-qc\]](#).
- [53] C. Chatterjee, L. Wen, D. Beveridge, F. Diakogiannis, and K. Vinsen, (2022), [arXiv:2207.14522 \[gr-qc\]](#).
- [54] C. Chatterjee and L. Wen, (2022), [arXiv:2301.03558 \[astro-ph.HE\]](#).
- [55] M. Dax, S. R. Green, J. Gair, M. Pürrer, J. Wildberger, J. H. Macke, A. Buonanno, and B. Schölkopf, *Phys. Rev. Lett.* **130**, 171403 (2023), [arXiv:2210.05686 \[gr-qc\]](#).
- [56] K. W. K. Wong, M. Isi, and T. D. P. Edwards, (2023), [arXiv:2302.05333 \[astro-ph.IM\]](#).
- [57] G. Vajente, Y. Huang, M. Isi, J. C. Driggers, J. S. Kissel, M. J. Szczepańczyk, and S. Vitale, *Phys. Rev. D* **101**, 042003 (2020), [arXiv:1911.09083 \[gr-qc\]](#).
- [58] R. Essick, P. Godwin, C. Hanna, L. Blackburn, and E. Katsavounidis, (2020), [arXiv:2005.12761 \[astro-ph.IM\]](#).
- [59] M. Saleem *et al.*, (2023), [arXiv:2306.11366 \[gr-qc\]](#).
- [60] S. Schmidt, M. Breschi, R. Gamba, G. Pagano, P. Rettigno, G. Riemenschneider, S. Bernuzzi, A. Nagar, and W. Del Pozzo, *Phys. Rev. D* **103**, 043020 (2021), [arXiv:2011.01958 \[gr-qc\]](#).
- [61] A. J. K. Chua, C. R. Galley, and M. Vallisneri, *Phys. Rev. Lett.* **122**, 211101 (2019), [arXiv:1811.05491 \[astro-ph.IM\]](#).
- [62] S. Khan and R. Green, *Phys. Rev. D* **103**, 064015 (2021), [arXiv:2008.12932 \[gr-qc\]](#).
- [63] J. Tissino, G. Carullo, M. Breschi, R. Gamba, S. Schmidt, and S. Bernuzzi, *Phys. Rev. D* **107**, 084037 (2023), [arXiv:2210.15684 \[gr-qc\]](#).
- [64] L. M. Thomas, G. Pratten, and P. Schmidt, *Phys. Rev. D* **106**, 104029 (2022), [arXiv:2205.14066 \[gr-qc\]](#).
- [65] K. Cannon, C. Hanna, and D. Keppel, *Phys. Rev. D* **85**, 081504 (2012), [arXiv:1108.5618 \[gr-qc\]](#).
- [66] L. Pathak, A. Reza, and A. S. Sengupta, (2022), [arXiv:2210.02706 \[gr-qc\]](#).
- [67] C. Messick *et al.*, *Phys. Rev. D* **95**, 042001 (2017), [arXiv:1604.04324 \[astro-ph.IM\]](#).
- [68] J. Roulet, L. Dai, T. Venumadhav, B. Zackay, and M. Zaldarriaga, *Phys. Rev. D* **99**, 123022 (2019), [arXiv:1904.01683 \[astro-ph.IM\]](#).
- [69] S. Sakon *et al.*, (2022), [arXiv:2211.16674 \[gr-qc\]](#).
- [70] K. Cannon, A. Chapman, C. Hanna, D. Keppel, A. C. Searle, and A. J. Weinstein, *Phys. Rev. D* **82**, 044025 (2010), [arXiv:1005.0012 \[gr-qc\]](#).
- [71] K. Cannon *et al.*, *Astrophys. J.* **748**, 136 (2012), [arXiv:1107.2665 \[astro-ph.IM\]](#).
- [72] T. Adams, D. Buskulic, V. Germain, G. M. Guidi, F. Marion, M. Montani, B. Mours, F. Piergiovanni, and G. Wang, *Class. Quant. Grav.* **33**, 175012 (2016), [arXiv:1512.02864 \[gr-qc\]](#).
- [73] K. Cannon, C. Hanna, and D. Keppel, *Phys. Rev. D* **84**, 084003 (2011), [arXiv:1101.4939 \[gr-qc\]](#).
- [74] I. Goodfellow, Y. Bengio, and A. Courville, *Deep Learning* (MIT Press, 2016) <http://www.deeplearningbook.org>.
- [75] D. P. Kingma and J. Ba (2014) [arXiv:1412.6980 \[cs.LG\]](#).
- [76] C. Cutler and E. E. Flanagan, *Phys. Rev. D* **49**, 2658 (1994), [arXiv:gr-qc/9402014](#).
- [77] S. Morisaki and V. Raymond, *Phys. Rev. D* **102**, 104020 (2020), [arXiv:2007.09108 \[gr-qc\]](#).
- [78] B. J. Owen and B. S. Sathyaprakash, *Phys. Rev. D* **60**, 022002 (1999), [arXiv:gr-qc/9808076](#).
- [79] I. W. Harry, B. Allen, and B. S. Sathyaprakash, *Phys. Rev. D* **80**, 104014 (2009), [arXiv:0908.2090 \[gr-qc\]](#).
- [80] S. Privitera, S. R. P. Mohapatra, P. Ajith, K. Cannon, N. Fotopoulos, M. A. Frei, C. Hanna, A. J. Weinstein, and J. T. Whelan, *Phys. Rev. D* **89**, 024003 (2014), [arXiv:1310.5633 \[gr-qc\]](#).
- [81] S. Sachdev *et al.*, (2019), [arXiv:1901.08580 \[gr-qc\]](#).
- [82] A. Bohé *et al.*, *Phys. Rev. D* **95**, 044028 (2017), [arXiv:1611.03703 \[gr-qc\]](#).
- [83] L. Blanchet, T. Damour, B. R. Iyer, C. M. Will, and A. G. Wiseman, *Phys. Rev. Lett.* **74**, 3515 (1995), [arXiv:gr-qc/9501027](#).
- [84] K. W. K. Wong, K. K. Y. Ng, and E. Berti, (2020), [arXiv:2007.10350 \[astro-ph.HE\]](#).
- [85] A. Olsson, G. Sandberg, and O. Dahlblom, *Structural Safety* **25**, 47 (2003).
- [86] T. D. P. Edwards, K. W. K. Wong, K. K. H. Lam, A. Coogan, D. Foreman-Mackey, M. Isi, and A. Zimmerman, (2023), [arXiv:2302.05329 \[astro-ph.IM\]](#).
- [87] J. Bradbury, R. Frostig, P. Hawkins, M. J. Johnson, C. Leary, D. Maclaurin, G. Necula, A. Paszke, J. VanderPlas, S. Wanderman-Milne, and Q. Zhang, “JAX: composable transformations of Python+NumPy programs,” (2018).
- [88] G. Ashton *et al.*, *Astrophys. J. Suppl.* **241**, 27 (2019), [arXiv:1811.02042 \[astro-ph.IM\]](#).
- [89] P. Canizares, S. E. Field, J. Gair, V. Raymond, R. Smith, and M. Tiglio, *Phys. Rev. Lett.* **114**, 071104 (2015), [arXiv:1404.6284 \[gr-qc\]](#).
- [90] R. Smith, S. E. Field, K. Blackburn, C.-J. Haster, M. Pürrer, V. Raymond, and P. Schmidt, *Phys. Rev. D* **94**, 044031 (2016), [arXiv:1604.08253 \[gr-qc\]](#).
- [91] C. A. Rose, V. Valsan, P. R. Brady, S. Walsh, and C. Pankow, (2022), [arXiv:2201.05263 \[gr-qc\]](#).
- [92] S. Morisaki, R. Smith, L. Tsukada, S. Sachdev, S. Stevenson, C. Talbot, and A. Zimmerman, (2023), [arXiv:2307.13380 \[gr-qc\]](#).
- [93] C. Pankow, P. Brady, E. Ochsner, and R. O’Shaughnessy, *Phys. Rev. D* **92**, 023002 (2015),

- [arXiv:1502.04370 \[gr-qc\]](#).
- [94] M. J. Berger and P. Colella, *Journal of Computational Physics* **82**, 64 (1989).
- [95] A. Tejero-Cantero, J. Boelts, M. Deistler, J.-M. Lueckmann, C. Durkan, P. J. Gonçalves, D. S. Greenberg, and J. H. Macke, *Journal of Open Source Software* **5**, 2505 (2020).
- [96] D. Chatterjee *et al.*, (2024), [arXiv:2407.19048 \[gr-qc\]](#).